Numerical Simulation of Aeroelastic Instabilities of Elementary Bridge Decks

Serge Piperno

INRIA

INSTITUT NATIONAL DE RECHERCHE EN INFORMATIQUE ET EN AUTOMATIQUE

Numerical simulation of aeroelastic instabilities of elementary bridge decks

Serge Piperno

N° 3549

Novembre 1998

THÈME 4

ISSN 0249-6399

INRIA
SOPHIA ANTIPOLIS

Numerical simulation of aeroelastic instabilities of elementary bridge decks

Serge Piperno

Thème 4 — Simulation et optimisation
de systèmes complexes
Projet Caiman

Rapport de recherche n° 3549 — Novembre 1998 — 35 pages

Abstract: In this report, we propose a global methodology for the numerical simulation of wind effects on elementary bridge profiles, particularly possible aeroelastic instabilities. This methodology is based on an efficient coupling algorithm, a finite-element solver for three-dimensional incompressible Navier-Stokes equations in a moving domain and a structural solver. The fluid solver is detailed, the emphasis being put on the ALE formulation. Numerical and experimental results are compared for cases with a structural rigid motion. On a rectangle, numerical simulations for forced oscillation (heaving or rotation) are qualitatively correct, rather inaccurate, but in good agreements with free oscillation numerical simulations though. On a H-shaped section close to the Tacoma Narrows bridge profile, numerical results are both qualitatively and quantitatively very satisfactory and promising.

Key-words: Fluid-structure interaction, wind effects, finite elements, ALE formulation, coupling algorithm, torsional flutter, vortex shedding.

Unité de recherche INRIA Sophia Antipolis
2004, route des Lucioles, B.P. 93, 06902 Sophia Antipolis Cedex (France)
Téléphone : 04 92 38 77 77 - International : +33 4 92 38 77 77 — Fax : 04 92 38 77 65 - International : +33 4 92 38 77 65

Simulation numérique d'instabilités aéroélastiques de profils de pont élémentaires

Résumé : Dans ce rapport, nous proposons une méthodologie globale pour la simulation numérique de l'effet du vent autour de profils de pont élémentaires, notamment l'apparition d'instabilités aéroélastiques. Cette méthodologie repose sur trois éléments essentiels: un algorithme de couplage, déjà utilisé en aérodynamique compressible, un solveur en éléments finis des équations de Navier-Stokes tridimensionnelles "incompressible" en domaine déformable et un solveur structure. Le solveur fluide est présenté en détail, notamment son implémentation en formulation ALE. On compare les résultats numériques à des résultats expérimentaux sur des cas-tests où la structure est en mouvement rigide. Sur un rectangle, les simulations numériques en mouvement forcé en translation ou rotation donnent des résultats encourageants, assez imprécis, néanmoins cohérents avec des simulations numériques en mouvement libre. Sur une section proche de celle du pont de Tacoma, les résultats sont qualitativement et quantitativement très prometteurs.

Mots-clés : interaction fluide-structure, effets du vent, élément fini, formulation ALE, algorithme de couplage, flottement en torsion, détachement tourbillonnaire.

Contents

1 Introduction **4**

2 Governing equations **5**
2.1 Structural models 5
2.2 Fluid equations 5

3 Numerical methods **7**
3.1 Structural time-integration 7
3.2 Fluid time and space discretizations 8
3.2.1 Time discretization of the original solver 8
3.2.2 Space discretization of the original solver 8
3.2.3 Derivation of the ALE solver 9
3.3 Coupling algorithm 11

4 Simulation results **11**
4.1 Fixed cylinders 12
4.1.1 Circular cylinder 12
4.1.2 Rectangular cylinder 14
4.2 Forced oscillation response of a rectangle cylinder 14
4.2.1 Heaving mode 14
4.2.2 Torsional mode 17
4.2.3 Conclusion 20
4.3 Free oscillation response of a rectangle cylinder 21
4.3.1 Heaving mode 21
4.3.2 Torsional mode 22
4.3.3 Conclusion 24
4.4 The Tacoma Narrows Bridge benchmark 26

5 Conclusion **34**

1 Introduction

Aeroelastic instabilities of civil engineering constructions such as suspension bridges and high-rise buildings have been the subjects of many experimental studies (see [15] for a collection of references). With the increase in computational power, the numerical simulation of such phenomena is now possible and some preliminary works have already been reported [6].

In this paper, we propose a set of numerical methods and algorithms to obtain efficient and accurate unsteady numerical simulations of aeroelastic instabilities of bluff bodies in a steady wind. The objective of this paper is to present and validate on preliminary simulations a global methodology. This global methodology is based on three main elements, which are the global coupling algorithm, the fluid flow solver and the structural solver. The global resolution is unsteady, no harmonic or modal assumptions are made. The coupling algorithm proposed in this paper was successfully developed for aerodynamic instabilities in compressible flows [10]. This staggered algorithm, i.e. the fluid and the structure are advanced in time successively and separately, was shown to be very accurate with time steps much larger than those used in this paper. The fluid solver deals with the incompressible Navier-Stokes equations in three dimensions and in a deforming domain. This necessary feature is implemented using an ALE reformulation of an existing code [8]. The structural solver is very simple, since this paper only deals with rigid sections of cylinders. The structural model itself is elementary (three degrees of freedom for rigid transverse motion of a section).

Our goal here is to numerically reproduce forced oscillation and free oscillation experiments of two benchmark sections : a rectangular cylinder of chord to thickness ratio equal to 4 and a cylinder with a H-section close to the profile of the Tacoma Narrows Bridge. These sections have been chosen because many experimental reports are available [12, 13, 15, 16]. For each cylinder and for each type of experience, numerical results are compared with experimental results. The quality of these numerical results as well as their computational cost are discussed.

In Section 2, we present the fluid and structural models, as well as the physical coupling of both systems. In Section 3, we describe the numerical methods used for the simulation. The flow is solved using a finite-element ALE solver, whereas the simple structural model is integrated using the trapezoidal rule. The coupling staggered algorithm is also given. In Section 4, we report numerical results for all benchmarks, including forced and free oscillation experiments on the rectangle and H-shaped cylinders. Finally, we conclude this paper in Section 5.

2 Governing equations

2.1 Structural models

In this paper, we only consider two-dimensional flexible structures in rigid motion. Such a structure plays the role of a section of a bridge deck. However, our global strategy can actually deal with linear, three dimensional structures in small displacements and deformations. The input data for such computations would be structural eigenmodes and eigenvalues, or complete mass and stiffness matrices. Extensions towards non-linear structures and large displacements and deformations should be added in an upgraded structural solver.

We collect here preliminary results on the numerical simulation of aeroelastic coupling of bridge decks in a constant wind, and the limitation to rigid motions of deck sections allows quick computations on a typical workstation. The structure is a simple bridge deck section (circular, rectangular or H-shaped cylinders) and is assumed rigid. The depth D of the section is fixed once and for all. Only two degrees of freedom are given: the vertical displacement y and the rotation θ around the center of rotation (which is also the center of symmetry). Equations for the evolutions of y and θ are written in a dimensional form:

$$\left\{ \begin{array}{rcl} m\ddot{y} + S_\theta \ddot{\theta} + c_y \dot{y} + k_y y & = & F_y \\ S_\theta \ddot{y} + I_\theta \ddot{\theta} + c_\theta \dot{\theta} + k_\theta \theta & = & M_\theta \end{array} \right. \tag{1}$$

where m, I_θ and S_θ denote respectively the mass of the section, and the inertial and static moments of the section around the elastic center; c_y and c_θ are damping coefficients for each degree of freedom, and k_y and k_θ are the corresponding stiffness coefficients. The profile is described on Figure 1.

Finally, F_y and M_θ are the lift and the moment (around the elastic center) exerted on the section by the fluid. The fluid force $\vec{F_{\mathbf{F}}}$ is exerted along the deck profile $\Gamma(t)$. It will be detailed later. The lift and moment are given by :

$$F_y = D \int_\Gamma \vec{F_{\mathbf{F}}}.\vec{e_y}\ ds \tag{2}$$

$$M_\theta = D \int_\Gamma \left(\vec{r} \times \vec{F_{\mathbf{F}}}\right).\vec{e_z}\ ds \tag{3}$$

where $\vec{r}$ is the location vector taken from the center of elasticity, as shown on Figure 1.

2.2 Fluid equations

We consider an external, viscous, incompressible flow around the deck section. Therefore, the three-dimensional fluid domain $\Omega(t)$, depicted in Figure 2, depends on time. The boundary $\partial\Omega(t)$ is made of two distinct parts: a far field boundary and the deck profile $\Gamma(t)$. Dirichlet type boundary conditions are assumed on both parts of $\partial\Omega(t)$. We set the following boundary conditions:

$$\left\{ \begin{array}{ll} \text{far field boundary } \Gamma_\infty : & \vec{\mathbf{u}}(t,\vec{x}) = \vec{\mathbf{u}}_\infty \\ \text{structural boundary } \Gamma(t) : & \vec{\mathbf{u}}(t,\vec{x}) = \vec{\mathbf{u}}_s(t,\vec{x}) \end{array} \right. , \tag{4}$$

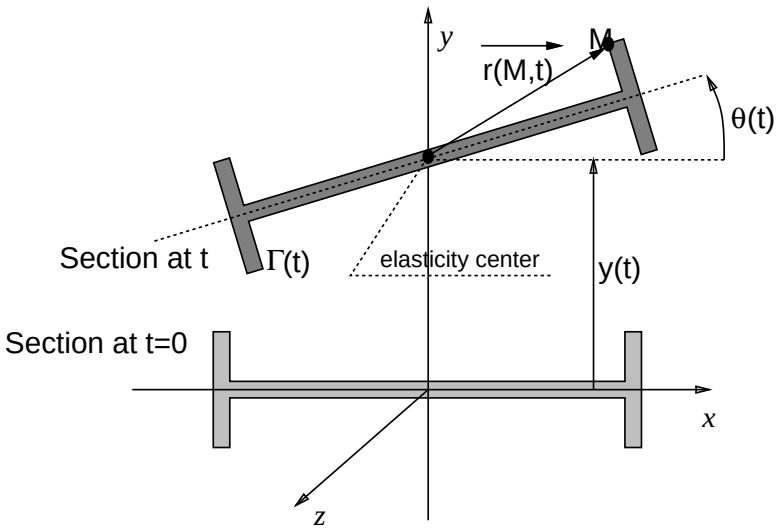

Figure 1: The two degree-of-freedom deck section.

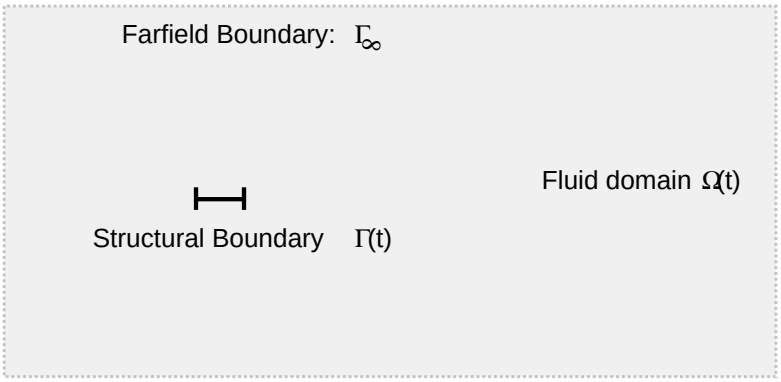

Figure 2: The time-varying fluid domain $\Omega(t)$.

where $\vec{\mathbf{u}}_\infty$ is a user set wind velocity and $\vec{\mathbf{u}}_s(t,\vec{x})$ is the structural speed at point $\vec{x}$ and at time t. The second boundary condition is a no slip condition on the fluid-structure interface. The fluid is governed by the unsteady incompressible Navier-Stokes equations in three dimensions

$$\begin{cases} \dfrac{\partial \vec{\mathbf{u}}}{\partial t} + (\vec{\mathbf{u}}.\nabla)\,\vec{\mathbf{u}} - \nu\Delta\vec{\mathbf{u}} + \nabla p = 0 \\ \nabla.\vec{\mathbf{u}} = 0 \end{cases} \tag{5}$$

where $\vec{\mathbf{u}}$ and p denotes respectively the fluid velocity and the reduced pressure (pressure divided by ρ_F). ν is the kinematic viscosity.

The dimensionalized fluid forces $\vec{F_{\mathbf{F}}}$ exerted on the structural surface ($\vec{n}$ denotes the local, external normal to the surface) depend on the pressure and the viscous stress terms.

$$\vec{F_{\mathbf{F}}} = \rho_F \left[-p\vec{n} + \nu\left(\nabla\vec{\mathbf{u}} + \nabla\vec{\mathbf{u}}^T\right)\ \vec{n}\right]. \tag{6}$$

3 Numerical methods

3.1 Structural time-integration

Whether the structural motion is rigid or it is decomposed along eigenmodes, the equations of motion can be rewritten into a second order differential equation of the form :

$$M_s\ddot{X} + D_s\dot{X} + K_sX = F, \tag{7}$$

where X is the vector of generalized coordinates (degrees of freedom, or modal coordinates), $\dot{X}$ and $\ddot{X}$ denote respectively the first and second time-derivatives of X, and M_s, D_s and K_s are mass, damping and stiffness generalized matrices. F is the vector of generalized fluid forces. For example, equations (1) yield

$$X = \begin{pmatrix} y \\ \theta \end{pmatrix},\ M_s = \begin{pmatrix} m & S_\theta \\ S_\theta & I_\theta \end{pmatrix},\ D_s = \begin{pmatrix} c_y & 0 \\ 0 & c_\theta \end{pmatrix},\ K_s = \begin{pmatrix} k_y & 0 \\ 0 & I_\theta \end{pmatrix},\ F = \begin{pmatrix} F_y \\ M_\theta \end{pmatrix}. \tag{8}$$

X^n, V^n, A^n and F^n are respectively numerical approximates for X, $\dot{X}$, $\ddot{X}$ and F at time $t^n = n\Delta t$. The time-integration of the structure is performed using the trapezoidal rule :

$$\begin{cases} X^{n+1} = X^n + \Delta t\frac{V^n + V^{n+1}}{2} \\ V^{n+1} = V^n + \Delta t\frac{A^n + A^{n+1}}{2} \\ M_sA^{n+1} + D_sV^{n+1} + K_sX^{n+1} = F^{n+1} \end{cases} \tag{9}$$

The trapezoidal rule is implicit, second-order accurate, and produces no artificial damping.

3.2 Fluid time and space discretizations

The fluid equations have to be solved in a moving domain. Thus we have to use an Arbitrary Lagrangian-Eulerian (ALE) approach. We have modified a hybrid P1-bubble/P1 finite-element solver, based on a purely Eulerian approach. We first give a description of this initial approach, and thereafter a quick derivation of the ALE solver.

3.2.1 Time discretization of the original solver

The momentum conservation equation can be rewritten using the material time derivative of the fluid velocity itself :

$$\frac{d}{dt}\left[\vec{\mathbf{u}}(t,\chi(t;s,x_0))\right] - \nu\Delta\vec{\mathbf{u}}(t,\chi(t;s,x_0)) + \nabla p(t,\chi(t;s,x_0)) = 0, \tag{10}$$

where χ is the Eulerian location of a characteristic curve for the fluid velocity field $\vec{\mathbf{u}}$, which is located at x_0 at time t_0, i.e.

$$\begin{cases} \dfrac{d}{dt}\left(\chi(t;t_0,x_0)\right) = \vec{\mathbf{u}}(t,\chi(t;t_0,x_0)), \\ \\ \chi(t_0;t_0,x_0) = x_0 \end{cases} \tag{11}$$

Thus the following time discretization is used : we assume we are able to backtrack the characteristic curve starting from any point x. We use a first-order backward Euler implicit scheme, which yields for the momentum and mass conservation equations

$$\begin{cases} \dfrac{\vec{\mathbf{u}}(t^{n+1},x) - \vec{\mathbf{u}}(t^n,\chi(t^n;t^{n+1},x))}{\Delta t} - \nu\Delta\vec{\mathbf{u}}(t^{n+1},x) + \nabla p(t^{n+1},x) = 0 \\ \\ \nabla.\vec{\mathbf{u}}(t^{n+1},x) = 0 \end{cases} \tag{12}$$

where Δt is the time step and $t^{n+1} = t^n + \Delta t$. The computation of upwind characteristics is based on an first-order time approximation. Each upwind characteristic is replaced by a polygonal chain of points located on faces of the unstructured mesh. Further details can be found in [8]. If the only term depending on $\vec{\mathbf{u}}(t^n,.)$ is put on the right hand side, the preceding equation takes the form of a generalized Stokes problem for the fields $\vec{\mathbf{u}}(t^{n+1},.)$ and $p(t^{n+1},.)$.

3.2.2 Space discretization of the original solver

The space discretization of the original solver is based on a classical P1-bubble/P1 hybrid finite element formulation. This element was chosen because of its good stability for a rather small number of degrees of freedom [1]. The computational domain is partitioned into tetrahedra, which form an unstructured tetrahedrization $\mathcal{T}_h$ of the domain, verifying classical regularity conditions for finite elements. Each component of the vector field $\vec{\mathbf{u}}$ is

a P1-bubble function. The pressure field p is a P1 function. The computational unknown at time t^n are the approximate functions $\vec{\mathbf{u}}_h(t^n,.)$ and $p_h(t^n,.)$, which are now denoted by $\vec{\mathbf{u}}^n$ and p^n, respectively. A variational formulation is derived from the generalized Stokes problem (12) and yields a linear system of the form

$$\begin{array}{c} A_h \vec{\mathbf{u}}_h^{n+1} + B_h p_h^{n+1} = F_h^{n+1} \\ \\ B_h^T \vec{\mathbf{u}}_h^{n+1} = X_h^{n+1} \end{array} , \tag{13}$$

where A_h is the symmetric definite positive matrix associated to the elliptic operator $k\,\mathbb{I} - \nu\Delta$, B_h is the matrix associated to pressure gradients, F_h^{n+1} and X_h^{n+1} are source terms deriving from the explicit term $\vec{\mathbf{u}}(t^n, \chi(t^n; t^{n+1}, x))$ in (12) and boundary conditions. The linear system (13) is solved with a Uzawa method [11], where the new linear system on p_h^{n+1} is iteratively solved with a preconditioned conjugate gradient algorithm [3]. All details on this algorithm can be found in [8].

3.2.3 Derivation of the ALE solver

The derivation of an ALE solver of Navier-Stokes equations for an incompressible viscous fluid is very simple. The fluid domain $\Omega(t)$ is deforming. Thus the tetrahedrization of the fluid domain must be modified at each time step. We have chosen a robust method proposed by Batina [2] and generalized by Lesoinne and Farhat [5]. Each vertex of the tetrahedrization is given the possibility to move, but the topology of the tetrahedrization remains fixed. The displacement of the structure on $\Gamma(t)$ (see Figure 2) is smoothly transmitted to internal grid points using an elastic analogy: edges of the tetrahedra are given a stiffness, and the static equilibrium of all vertices is seeked for. All details can be found in [10].

Equations (12) are purely Eulerian, since the field $\vec{\mathbf{u}}$ and p are Eulerian, and depend on the coordinate x in the laboratory. The time scheme must be rewritten in moving coordinates ξ. For any ξ, i.e. for any grid point, we denote by $x(t^n, \xi)$ its Eulerian position at time t^n. We also replace $z(t, x(t, \xi))$ by $z(t, \xi)$ for any quantity z. Equations (12) can now be rewritten for any ξ as

$$\left\{ \begin{array}{l} \dfrac{\vec{\mathbf{u}}\left(t^{n+1}, \xi\right) - \vec{\mathbf{u}}\left(t^n, \chi(t^n; t^{n+1}, x(t^{n+1}, \xi))\right)}{\Delta t} - \nu\Delta\vec{\mathbf{u}}\left(t^{n+1}, \xi\right)) + \nabla p\left(t^{n+1}, \xi\right)) = 0 \\ \\ \nabla.\vec{\mathbf{u}}(t^{n+1}, \xi) = 0 \end{array} \right.$$

If we omit the term $\vec{\mathbf{u}}\left(t^n, \chi(t^n; t^{n+1}, x(t^{n+1}, \xi))\right)$ in the preceding equation, we find again a generalized Stokes problem in the configuration of the moving grid at time t^{n+1}. Therefore, the derivation of an ALE solver is straightforward. One time integration from time t^n to time t^{n+1} is done the following way:

Step 1 - Compute the vector field $\vec{\mathbf{v}}$ of velocities of all vertices for the current time step,

Step 2 - Update the mesh by moving the grid points,

Step 3 - Update all finite element matrices involved in (13) depending on the geometry,

Step 4 - Compute the characteristic term deriving from $\vec{\mathbf{u}}\left(t^n, \chi(t^n; t^{n+1}, x(t^{n+1}, \xi))\right)$,

Step 5 - solve the generalized Stokes problem in the new configuration.

The derivation of an ALE solver will be completed when we have described the computation of the right hand term deriving from $\vec{\mathbf{u}}\left(t^n, \chi(t^n; t^{n+1}, x(t^{n+1}, \xi))\right)$. This value is not directly accessible in the solver, since $\chi(t^n; t^{n+1}, x(t^{n+1}, \xi))$ is an Eulerian coordinate. We propose to find a moving coordinate $\bar{\xi}$, such that

$$\chi\left(t^n; t^{n+1}, x(t^{n+1}, \xi)\right) \sim x(t^n, \bar{\xi}). \tag{14}$$

That way, we have

$$\vec{\mathbf{u}}\left(t^n, \chi(t^n; t^{n+1}, x(t^{n+1}, \xi))\right) \sim \vec{\mathbf{u}}\left(t^n, x(t^n, \bar{\xi})\right) \equiv \vec{\mathbf{u}}\left(t^n, \bar{\xi}\right),$$

the last term being a directly accessible computational value before the field $\vec{\mathbf{u}}$ is updated in the last step (even after the mesh has been updated, i.e. the Eulerian coordinates of vertices have been changed). We propose to choose $\bar{\xi}$ such that $x(t^{n+1}, \bar{\xi}) = \bar{\chi}\left(t^n; t^{n+1}, x(t^{n+1}, \xi)\right)$ with

$$\begin{cases} \dfrac{d}{dt}\left(\bar{\chi}(t; s, x_0)\right) = \vec{\mathbf{u}}(t, \bar{\chi}(t; s, x_0)) - \vec{\mathbf{v}}(t, \bar{\chi}(t; s, x_0)), \\ \\ \bar{\chi}(s; s, x_0) = x_0 \end{cases} \tag{15}$$

The approximation (14) holds at the first order in Δt since we have

$$\chi\left(t^n; t^{n+1}, x(t^{n+1}, \xi)\right) = x(t^{n+1}, \xi) - \Delta t\ \vec{\mathbf{u}}\left(t^n, x(t^{n+1}, \xi)\right) + \mathcal{O}(\Delta t^2) \tag{16a}$$

$$x(t^{n+1}, \bar{\xi}) = x(t^{n+1}, \xi) - \Delta t\ \left(\vec{\mathbf{u}} - \vec{\mathbf{v}}\right)\left(t^n, x(t^{n+1}, \xi)\right) + \mathcal{O}(\Delta t^2) \tag{16b}$$

$$x(t^n, \bar{\xi}) = x(t^{n+1}, \bar{\xi}) - \Delta t\ \vec{\mathbf{v}}\left(t^n, x(t^{n+1}, \xi)\right) + \mathcal{O}(\Delta t^2) \tag{16c}$$

Equation (16a) derives from the definition (11) of the characteristic $\chi(.; t^{n+1}, x(t^{n+1}, \xi))$ for the field $\vec{\mathbf{u}}$. Similarly, equation (16b) derives from the definition (15) of the modified characteristic $\bar{\chi}(.; t^{n+1}, x(t^{n+1}, \xi))$ for the field $\vec{\mathbf{u}} - \vec{\mathbf{v}}$. Finally, equation (16c) derives from the definition of the mesh motion and from equation (16b) which yields $\bar{\xi} = \xi + \mathcal{O}(\Delta t)$.

To make things short, the Step 4. of the proposed algorithm is done the following way. For each mixed coordinate ξ,

Step 4a - backtrack over Δt the modified characteristic curve $\bar{\chi}$ starting from ξ. This can be done in the mesh configuration at time t^{n+1}.

Step 4b - compute the mixed coordinate $\bar{\xi}$ in the mesh configuration at time t^{n+1} of the point obtained,

Step 4c - get the not yet updated value $\vec{\mathbf{u}}(t^n, \bar{\xi})$.

3.3 Coupling algorithm

In this work, we have used a very simple coupling algorithm. Our main goal was the physical validation of the coupled code. Thus, we have used rather small time steps for both the fluid and the structure, and the coupling scheme should not be a crucial point.

We use a staggered coupling algorithm, where the fluid and the structure are advanced in time separately and successively. Although the time step is always small, we have a staggered algorithm which can be used up to thirty time steps per period of coupled oscillation [9]. The coupled algorithm, for a time integration from time t^n to time $t^{n+1} = t^n + \Delta t$, is the following:

I. Compute the following prediction for the structure at time t^{n+1}

$$\tilde{X}^{n+1} = X^n + \frac{\Delta t}{2}\left(3V^n - V^{n-1}\right).$$

II. From $\tilde{X}^{n+1}$, deduce a prediction for the location of the fluid-structure interface $\Gamma(t^{n+1})$.

III. Propagate the displacement to internal fluid vertices. Store the grid velocities $\vec{\mathbf{v}}$.

IV. Advance the fluid from t^n to t^{n+1} using the fluid ALE solver.

V. Compute the fluid forces $\vec{F}_{\mathbf{F}}^{\,n+1}$ of (6) on the structure at time t^{n+1} and the corresponding generalized forces $F_{\mathbf{F}}^{n+1}$ given by (8), (2) and (3).

VI. Advance the structure with the trapezoidal rule (9) and with the forces F^{n+1} given by

$$F^{n+1} = 2F_{\mathbf{F}}^{n+1} - F^n.$$

Note that with this algorithm, the matching condition on the fluid and structural boundaries is relaxed : at the end of the current time step, the fluid boundary $\Gamma(t^{n+1})$ matches the second-order accurate prediction $\tilde{X}^{n+1}$, which is different from the result of the structural integration X^{n+1}.

4 Simulation results

In this section, we review numerical results obtained for several test cases. We first consider fixed cylinders, which are very good benchmarks for the fixed grid fluid solver, and for the computation of fluid forces on the structure.

We then study the oscillation responses of a rectangle cylinder. We compare aeroelastic analyses based on numerical simulations and physical experiences, for both forced and free oscillations.

Finally, we investigate the aeroelastic response of a simplified Tacoma Narrows Bridge deck for different constant wind speeds.

4.1 Fixed cylinders

We validate the fluid solver on a fixed grid, as well as the computation of lift and moment coefficients for simple structural models.

4.1.1 Circular cylinder

We first consider the unsteady laminar flow of a viscous incompressible fluid past a circular cylinder of radius $R = 1m$. We have used $u_\infty = 1m/s$ and $\nu = 0.01m^2/s$, which sets the Reynolds numbers (based on the diameter $D = 2R$ of the cylinder) to $Re = 200$. Both numerical and experimental results for this test case are reviewed in [4]. We have chosen to take the Stokes flow as initial value at time $t = 0s$.

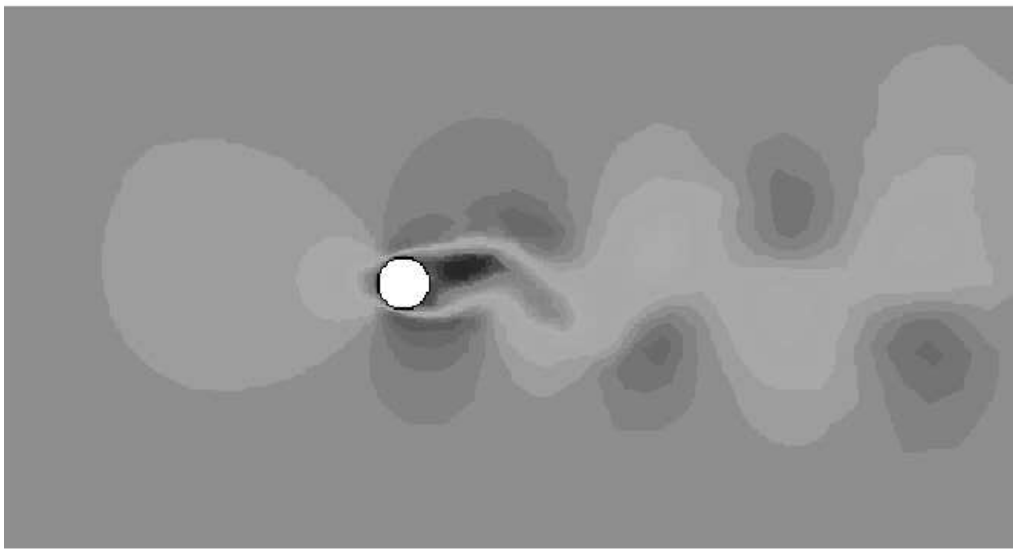

Figure 3: Horizontal velocity (fixed circular cylinder)

After a transient phase, a periodic vortex shedding appears. The horizontal velocity of the fluid is shown on Figure 3. The corresponding Strouhal number is defined by $S =$

fD/u_∞, where f is the dimensional frequency of the vortex shedding. The unsteady lift and drag coefficients (per unit span) are plotted on Figure 4. These adimensional coefficients are respectively given by

$$C_x = \frac{\vec{F_{\mathbf{F}}}.\vec{e_x}}{0.5\rho_\infty u_\infty^2 D} \quad C_y = \frac{\vec{F_{\mathbf{F}}}.\vec{e_y}}{0.5\rho_\infty u_\infty^2 D} \tag{17}$$

where the density ρ_∞ is the constant density of the incompressible flow. Classically, f is the frequency f_y of oscillations for the lift coefficient C_y. It is commonly observed that the frequency f_x of oscillations of the drag coefficient C_x is approximatively $f_x = 2f_y$. This is also the case for the numerical results (see Figure 4).

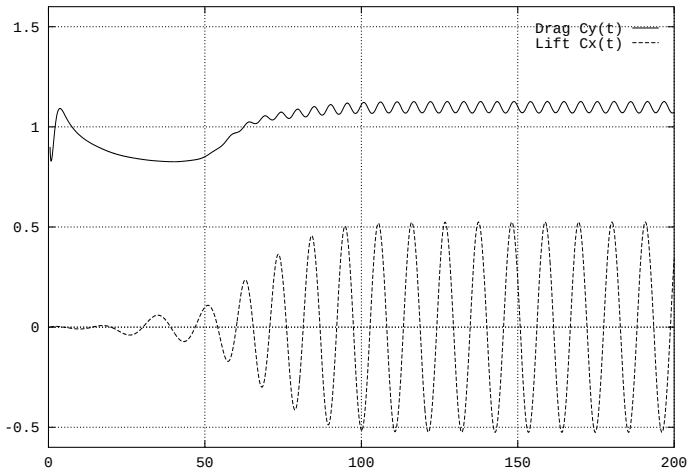

Figure 4: Lift and drag coefficients (fixed circular cylinder)

The numerical results for the fixed circular cylinder are in very good agreement with the results reviewed in [4]. For several values of the time step Δt, the numerical results for S, as well as the average values and amplitudes for the lift and drag coefficients are reported on Table 1. They are compared with the averages of values reported in [4]. The values obtained by the fluid solver are in the range of other numerical and experimental values. It can be noticed that the time step Δt has some (limited) influence on numerical results. This is probably due to the method of characteristics chosen for the treatment of the non-linear advection term. As the time step increases, the second-order error in characteristic curves becomes preponderant.

Table 1: Numerical and experimental values for S, C_x and C_y (fixed circular cylinder)

	C_x	C_y	Strouhal S
$\Delta t = 0.05s$	1.242 ± 0.029	± 0.546	0.188
$\Delta t = 0.10s$	1.253 ± 0.029	± 0.535	0.181
$\Delta t = 0.15s$	1.265 ± 0.028	± 0.518	0.175
Numerical results [4]	$[1.17 - 1.58] \pm [0.035 - 0.04]$	$\pm[0.4 - 0.7]$	$[0.15 - 0.194]$
Experimental results [4]	1.30		$[0.16 - 0.19]$

4.1.2 Rectangular cylinder

We reproduce the same type of numerical simulations for a fixed rectangular cylinder. We consider a rectangle of chord to thickness ratio c/d equal to 4 (c denotes the chord, the length of the rectangular deck in the direction of the uniform flow, and d is the thickness of the deck in the perpendicular direction). The fluctuation of the flow in the wake behind the stationary rectangle has also a periodic behaviour after a transient phase. The periodic vortex shedding is again characterized by the Strouhal number $S = fd/u_\infty$. We consider experiments with a Reynolds number based on the thickness d $Re \equiv du_\infty/\nu = 20000$ ($d = 1m$, $u_\infty = 1m/s$, $\nu = 0.00005$). No turbulence model are used in the computations.

The unsteady lift and drag coefficients (per unit span) are plotted on Figure 5. These adimensional coefficients are now given by

$$C_x = \frac{\vec{F}_{\mathbf{F}}.\vec{e}_x}{0.5\rho_\infty u_\infty^2 c} \quad C_y = \frac{\vec{F}_{\mathbf{F}}.\vec{e}_y}{0.5\rho_\infty u_\infty^2 c} \tag{18}$$

where the density ρ_∞ is the constant density of the incompressible flow. Again, the shedding frequency f is equal to the frequency of lift oscillations, and equal to the half of the frequency of drag oscillations (see Figure 5).

Numerical simulations with the Eulerian code give $S = 0.128$, which is in very good agreement with the value given by experiments [7], which is $S \sim 0.13$.

4.2 Forced oscillation response of a rectangle cylinder

4.2.1 Heaving mode

In this section, we aim at reproducing experimental results reported by Washizu *et al.* [15]. With numerical simulations of forced oscillations in a heaving mode, we want to study the aeroelastic instability of a rectangle cylinder of chord to thickness ratio c/d equal to 4. The cylinder (see Figure 1) is given a forced sinusoidal oscillation

$$y(t) = y_m \cos(\omega_m t) \tag{19}$$

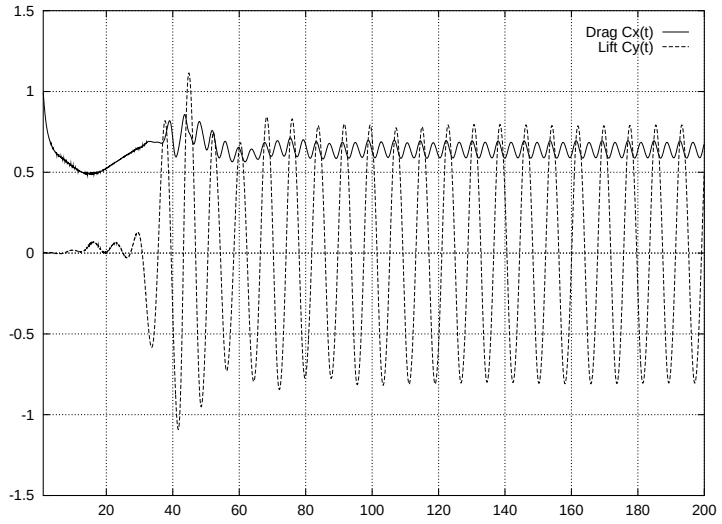

Figure 5: Lift and drag coefficients (fixed rectangular cylinder with $c/d = 4$)

and the resulting aerodynamic lift force $L(t)$ is computed over a certain number of periods $T_m = 2\pi/\omega_m$. The frequency response part $L_m(t)$ of the signal $L(t)$ is well described in [7]. We recall here the main points. $L_m(t)$ is defined by

$$L_m(t) = L_{mR}\cos(\omega_m t) - L_{mI}\sin(\omega_m t), \tag{20}$$

$$\text{with } [L_{mR}, L_{mI}] = \frac{1}{T}\int_{-T}^{T} L(t)[\cos(\omega_m t), \sin(\omega_m t)]\, dt. \tag{21}$$

The integration is extended over a great number of periods (typically $T = 30T_m$). It is frequently found convenient to deal with non-dimensional lift coefficients (per unit span) C_{LmR} and C_{LmI} defined by

$$\begin{cases} L_{mR} = 0.5\ \rho_\infty u_\infty^2 c\ C_{LmR}, \\ L_{mI} = 0.5\ \rho_\infty u_\infty^2 c\ C_{LmI}. \end{cases} \tag{22}$$

The non-dimensional numbers C_{LmR} and C_{LmI} give informations on the effect of aerodynamic forces on the profile, when it is moving in a heaving mode with pulsation ω_m. More precisely, if the coefficient C_{LmR} is positive (respectively negative), the fluid plays the role of an added mass (respectively an added stiffness). The damping effect of the fluid on the structure is directly related to the coefficient C_{LmI}. If $C_{LmI} < 0$, the fluid receives energy from the structure. It plays an actual damping role and the frequency analysis will conclude the structure is stable. On the contrary, if $C_{LmI} > 0$, the fluid transmits energy to the structure. It is a source of negative damping and the frequency analysis will conclude the structure is unstable.

The frequency response part analysis can be performed for different values of y_m and ω_m in (19). The reduced velocity $\mathbf{v}_m = u_\infty T_m/d$ is usually preferred to the dimensional pulsation ω_m. We first report here numerical results for $y_m = 2cm$ and $\mathbf{v}_m$ in the range $[5 : 40]$. The numerical results reported here were obtained after one simulation (with 12 successive periodic regimes and $T = 20T_m$ in each regime) of $60h$ on a Sun Ultra 170 workstation. The computations were made on a 2830-vertex, 7428-tetrahedron unstructured mesh. The three dimensional domain represents a one meter slice around a one meter span section of the rectangular cylinder.

The coefficients C_{LmR} obtained with our ALE fluid solver and obtained by experiments [15] are shown on Figure 6. The numerical results for C_{LmR} are qualitatively correct. The

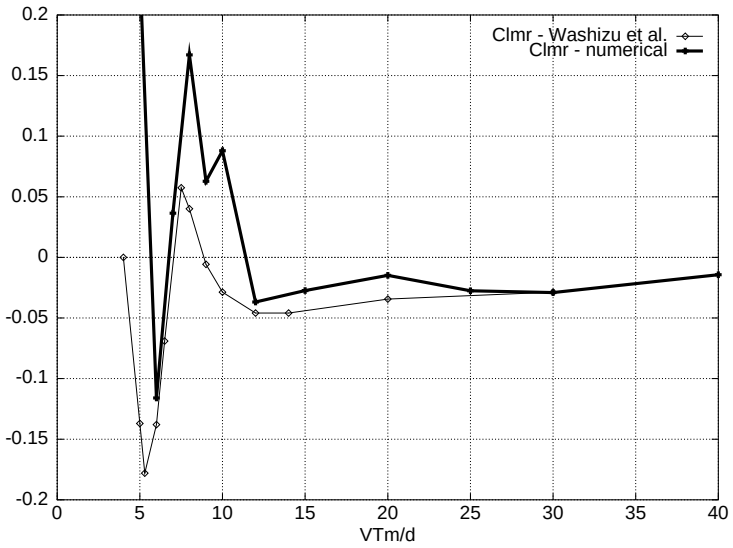

Figure 6: Coefficients C_{LmR} for $y_m = 2cm$ (numerical simulations and [15]).

oscillations in the range $\mathbf{v}_m \in [5 : 10]$ are present, and the behaviour for $\mathbf{v}_m > 25$ is well reproduced. However, the numerical results are far from perfect, since some additional oscillations are present.

The coefficients C_{LmI} obtained by both numerical simulations and experiments are shown on Figure 7. The numerical results are not accurate. The numerical curve seems to be shifted in the direction of larger $\mathbf{v}_m$. However, both curves give comparable stability results for this rectangular deck in a heaving mode. Experiments predict the deck is stable for all regimes, the ranges $\mathbf{v}_m < 4$ and $\mathbf{v}_m \in [6 : 7.5]$ excepted, while the present numerical simulation predicts instability in the ranges $\mathbf{v}_m < 6$ and $\mathbf{v}_m \in [7.5 : 12]$. For these simulations, the time step used by the ALE fluid solver was $\Delta t = 0.1s$, which corresponds to fifty time steps per period for the smallest period $T_m = 5$. Thus, the time step does not seem to be at the origin of the $\mathbf{v}_m$ shift between the two curves.

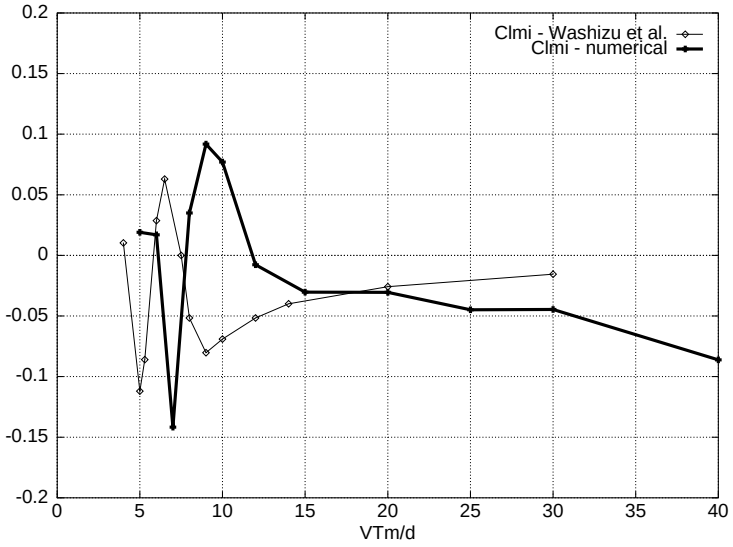

Figure 7: Coefficients C_{LmI} for $y_m = 2cm$ (numerical simulations and [15]).

We now report the same sets of results for $y_m = 10cm$ (the numerical results were also obtained after one $60h$ run on a Sun Ultra 170 workstation).

The coefficients C_{LmR} obtained by experiments [15] and numerics are shown on Figure 8. The numerical results are qualitatively acceptable. The oscillations in the range $\mathbf{v}_m \in [5:10]$ are again present, and the behaviour for $\mathbf{v}_m > 15$ is well reproduced. However, the numerical results are far from perfect, since the sign of the numerical C_{LmR} is wrong in the range $\mathbf{v}_m \in [6:11]$

The coefficients C_{LmI} obtained by both numerical simulations and experiments are shown on Figure 9. The numerical results are quite accurate. The dip in the range $\mathbf{v}_m \in [5:9]$ is well reproduced, as well as the low frequency behaviour in the range $\mathbf{v}_m < 15$ (however, the computational value for $\mathbf{v}_m = 40$ is suspect). Furthermore, the overall stability of the rectangular cylinder in the whole range $\mathbf{v}_m \in [5:40]$ is numerically predicted.

4.2.2 Torsional mode

In this section, we aim at reproducing experimental results reported by Washizu *et al.* [16]. We perform numerical simulations of forced oscillations in a torsional mode of the same rectangle cylinder ($c/d = 4$). The cylinder (see Figure 1) is given a forced sinusoidal oscillation

$$\theta(t) = \theta_m \cos(\omega_m t) \tag{23}$$

and the resulting aerodynamic moment $M(t)$ is computed over a certain number of periods $T_m = 2\pi/\omega_m$. The frequency response part $M_m(t)$ of the signal $M(t)$ is defined as previously

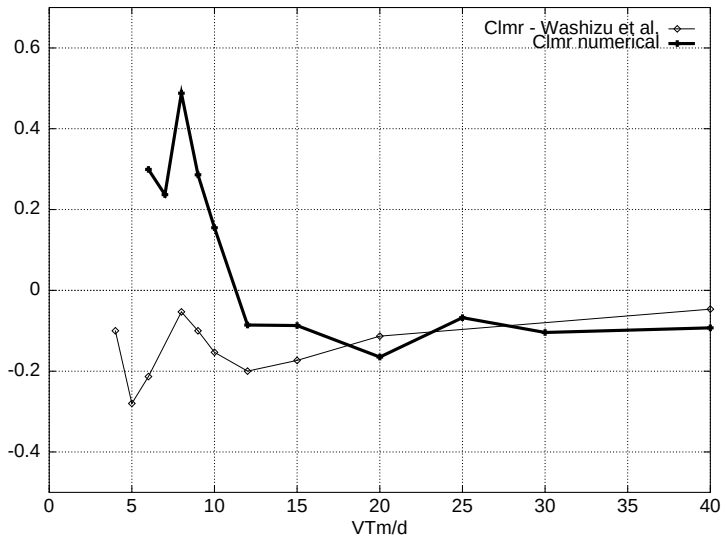

Figure 8: Coefficients C_{LmR} for $y_m = 10cm$ (numerical simulations and [15]).

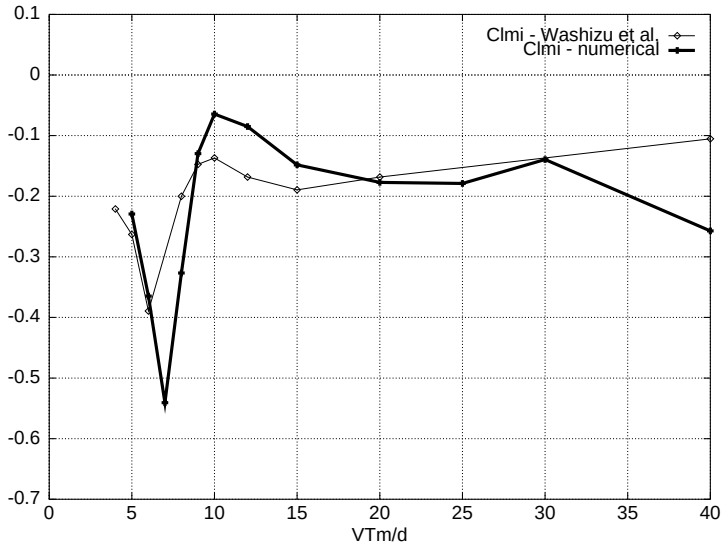

Figure 9: Coefficients C_{LmI} for $y_m = 10cm$ (numerical simulations and [15]).

for $L_m(t)$, yielding the two dimensional quantities M_{mR} and M_{mI}. The integration is extended over a great number of periods (typically $T = 30T_m$). We now deal with non-dimensional moment coefficients (per unit span) C_{MmR} and C_{MmI} defined by

$$\begin{cases} M_{mR} = 0.5\ \rho_\infty u_\infty^2 c^2\ C_{MmR}, \\ M_{mI} = 0.5\ \rho_\infty u_\infty^2 c^2\ C_{MmI}. \end{cases} \tag{24}$$

Again, the non-dimensional numbers C_{MmR} and C_{MmI} give informations on the effect of aerodynamic forces on the profile, when it is moving in a torsional mode with pulsation ω_m. The coefficient C_{MmR} represents a fluid added mass (respectively a fluid added stiffness) whenever it is positive (respectively negative). The damping effect of the fluid on the structure is directly related to the coefficient C_{MmI}. As previously, if $C_{MmI} > 0$, the fluid transmits energy to the structure. It is a source of negative damping and the frequency analysis will conclude the structure is unstable.

The frequency response part analysis is performed with $\theta_m = 1.91$ deg for different values of ω_m in the range $[5 : 40]$ (numerical results obtained after one $60h$ run on a Sun Ultra 170 workstation).

The coefficients C_{MmR} obtained with our ALE fluid solver and obtained by experiments [16] are shown on Figure 10. The numerical results for C_{LmR} are in very good agreement

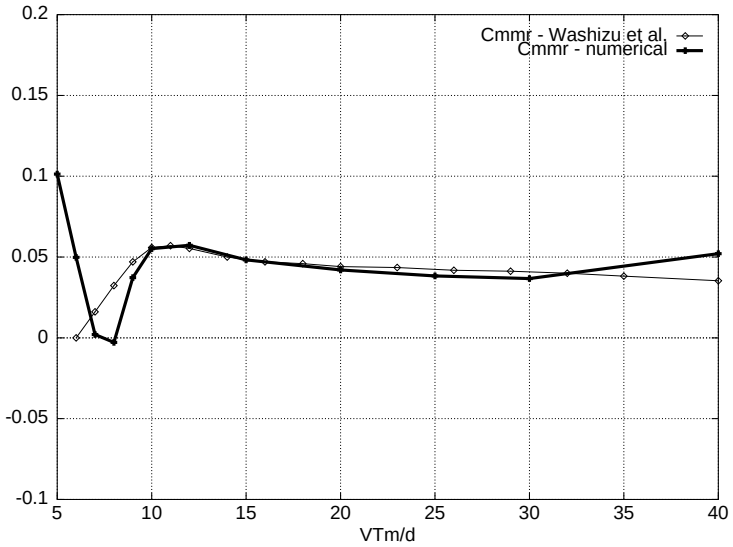

Figure 10: Coefficients C_{MmR} for $\theta_m = 1.91$ deg (numerical simulations and [16]).

with the experimental results. The dip in the range $\mathbf{v}_m \in [5 : 10]$ is present, and the behaviour for $\mathbf{v}_m > 10$ is very well reproduced.

The coefficients C_{MmI} obtained by both numerical simulations and experiments are shown on Figure 11. The numerical results are quite accurate. The numerical curve seems

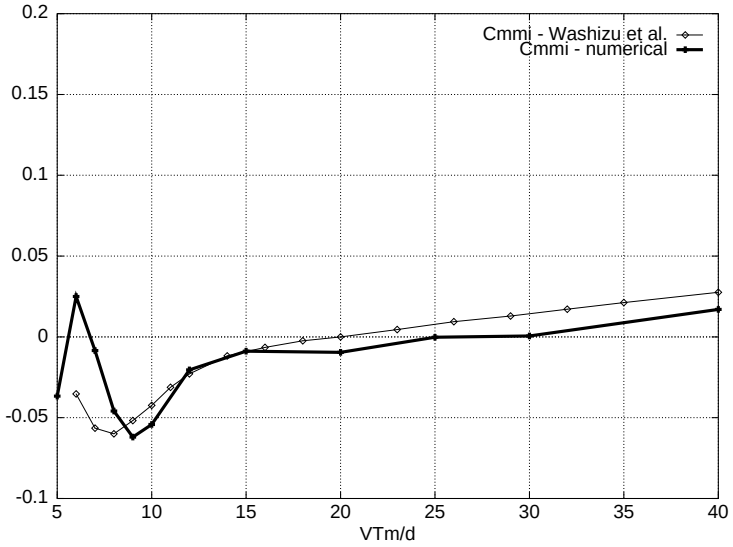

Figure 11: Coefficients C_{MmI} for $\theta_m = 1.91$ deg (numerical simulations and [16]).

slightly shifted in the direction of larger $\mathbf{v}_m$. However, both curves give comparable stability results for this rectangular deck in a torsional mode. Experiments predict the deck is unstable for $\mathbf{v}_m > 20$, while the present numerical simulation predicts instability for $\mathbf{v}_m > 25$. The numerical result for $\mathbf{v}_m \leq 6$ (high frequencies) might be related to a time step $\Delta t = 0.1s$ too large and the result for $\mathbf{v}_m = 40$ is again rather strange.

4.2.3 Conclusion

The numerical results presented here for forced oscillations yield satisfactory predictions on the possible instability of the rectangular cylinder. For the heaving mode, an instability at $y_m = 2cm$ in the range $\mathbf{v}_m \in [5 : 10]$ was correctly predicted, as well as the overall stability at $y_m = 10cm$. For the torsional mode, numerical simulation have given even more accurate predictions on the instability of the rectangular profile beyond a stability limit. This limit was experimentally observed round $\mathbf{v}_m = 20$, while numerical simulations predicted $\mathbf{v}_m = 25$. The reader should keep in mind these discrepancies can have multiple origins, lack of turbulence models, computational constraints on the space discretization and the time step Δt to name a few.

4.3 Free oscillation response of a rectangle cylinder

In this section, we would like to test the fluid-structure solver on free oscillation experiments. We consider test cases for which simulation results can be compared with results of forced oscillation experiments.

4.3.1 Heaving mode

We consider the following test case. The rectangle cylinder is given the ability to move freely in the vertical direction (rigid motion). We have noticed that, for forced oscillations at $\mathbf{v}_m = 10$, the fluid has a stabilizing effect for $y_m = 10cm$ and a destabilizing effect for $y_m = 2cm$. This means that a free oscillation experiment should lead to oscillations of amplitude between $2cm$ and $10cm$.

We propose a simulation with the following parameters : $c = 4m$, $d = 1m$, $u_\infty = 1m/s$, $Re = 20000$ ($\nu = 0.00005$) and, in (1), $\theta(t) \equiv 0$, $m = 100kg$, $c_y = 0$, $k_y = m\omega_s^2$. The structural pulsation ω_s is taken such that $T_s = 2\pi/\omega_s = 10s$, which yields $u_\infty T_s/d = 10$. The vertical displacement $y(t)$ is forced to $y(t) = y_0 \sin(\omega_s t)$ during ten structural periods T_s. Then the structure is released.

We first test $y_0 = 20cm$. The vertical displacement $y(t)$ and the structural energy $e(t) = (m\dot{y}^2(t) + k_y y^2(t))/2$ are respectively plotted on Figure 12 and Figure 13 in function of the time t. During ten periods (until $t = 100s$), the amplitude of the displacement and

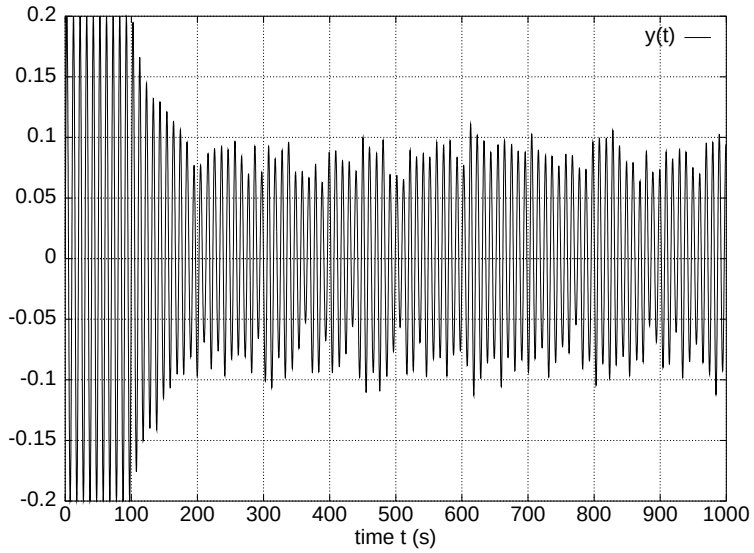

Figure 12: Vertical displacement for free oscillations ($y_0 = 20cm$, $T_s = 10s$).

the energy are held constant. When the structure is released, the amplitude of oscillation

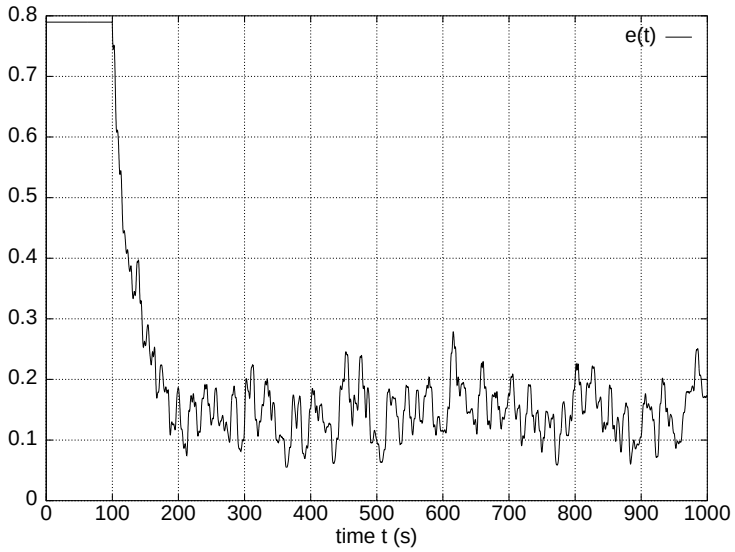

Figure 13: Structural energy for free oscillations ($y_0 = 20cm$, $T_s = 10s$).

decreases and a certain part of the structural energy is transmitted to the fluid. The stabilizing effect of the fluid (in at least the range $y_0 \in [10cm; 20cm]$) has been demonstrated. After a transient phase, the system evolves in an aperiodic limit cycle, where the displacement amplitude is less than $10cm$.

We now try $y_0 = 5cm$. The vertical displacement $y(t)$ and the structural energy are respectively plotted on Figure 14 and Figure 15 in function of the time t. In that case, after the structure is released, the amplitude of oscillation increases and a certain part of the structural energy is transmitted by the fluid. The destabilizing effect of the fluid (in at least the range $y_0 \in [2cm; 5cm]$) has again been recovered. After a transient phase, the system evolves in an aperiodic limit cycle, where the displacement amplitude is also less than $10cm$.

Since the rectangular cylinder is stable for any reduced velocity (see Figure 9) at $y_m = 10cm$, we can reproduce the preceding experience with $y_0 = 10cm$ and different values of T_s in the range $[5 : 40]$. For each T_s, we have plotted on Figure 16 the average structural energy after a pseudo-limit cycle is obtained. The average energy is of course bounded for all values of T_s. One can notice the strong resonance at $T_s = 10s$. This kind of lock in could be a source of fatigue for flexible structures like a suspended span bridge in a transverse wind.

4.3.2 Torsional mode

The rectangle cylinder is now given the ability to rotate freely (rigid motion, with $y \equiv 0$). We use the same parameters as previously, except for the structure : $y(t) \equiv 0$, $I_\theta = 100kg.m^2$,

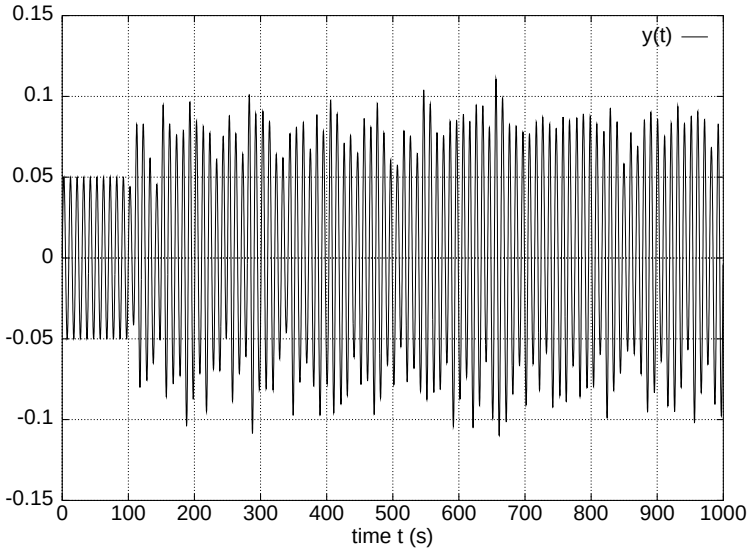

Figure 14: Vertical displacement for free oscillations ($y_0 = 5cm$, $T_s = 10s$).

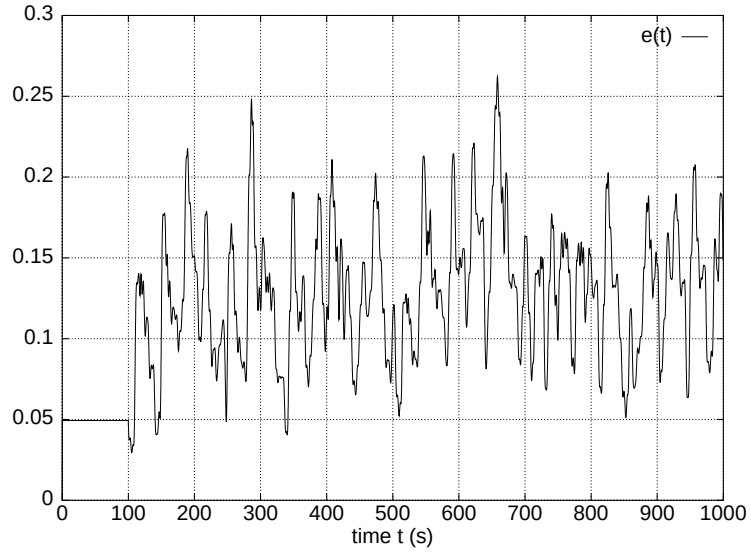

Figure 15: Structural energy for free oscillations ($y_0 = 5cm$, $T_s = 10s$).

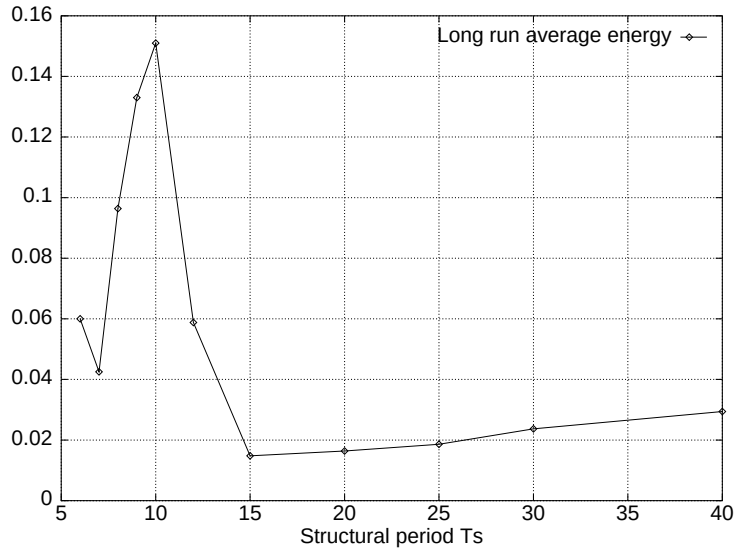

Figure 16: Long-run average structural energy for free heaving.

$c_\theta = 0$, $k_\theta = I_\theta \omega_s^2$ in (1). For different values of $T_s = 2\pi/\omega_s$ in the range $[5 : 40]$, we reproduce the following numerical simulation : the rotation $\theta(t)$ is forced to $y(t) = \theta_0 \sin(\omega_s t)$ during ten structural periods T_s (with $\theta_0 = 1.91$ deg). Then the structure is released.

For each $T_s < 15s$, the amplitude of oscillations is bounded. However, as T_s increases, the motion of the rectangle gets less periodic. We have plotted on Figure 17 the average and maximal structural energy ($e(t) = (I_\theta \dot{\theta}^2(t) + k_\theta \theta^2(t))/2$ after a pseudo-limit cycle is obtained. The average energy seems constant for $8 < T_s < 15$, but the maximal energy (reached randomly) increases. This is confirmed by the fact that, for $T_s = 15s$, the rotation θ and the energy get unbounded, as shown respectively on Figure 18 and Figure 19. This kind of lock in could be a source of collapse for flexible structures like a suspended span bridge in a transverse wind. We have plotted on Figure 20 pressure contours at a time with maximal rotation as the instability develops. One can notice the darker zone of low pressure under the rectangle, which clearly has a destabilizing effect (the resulting moment $M(t)$ has the same sign as $\theta(t)$).

4.3.3 Conclusion

The results presented in this section show a very good coherence between the forced and free oscillation analyses based on numerical results. We now want to test our coupled solver on more complex geometries. We have chosen to investigate the aerodynamic stability of the Tacoma Narrows Bridge.

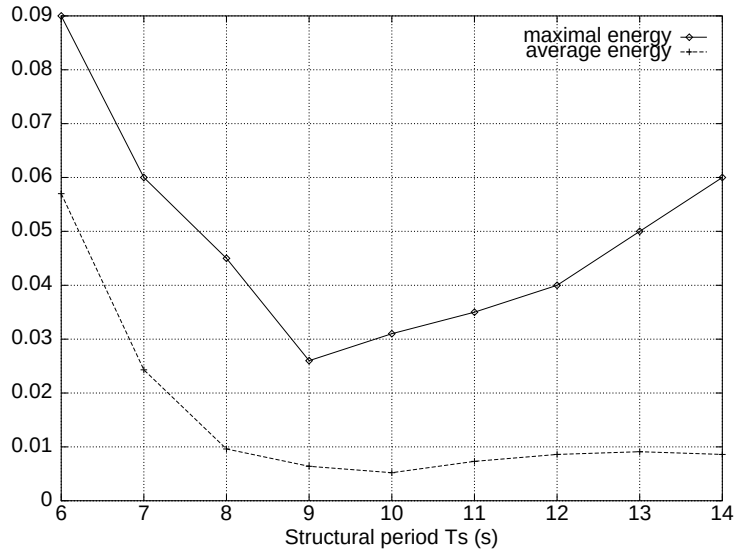

Figure 17: Long-run average and maximal structural energy for free rotation.

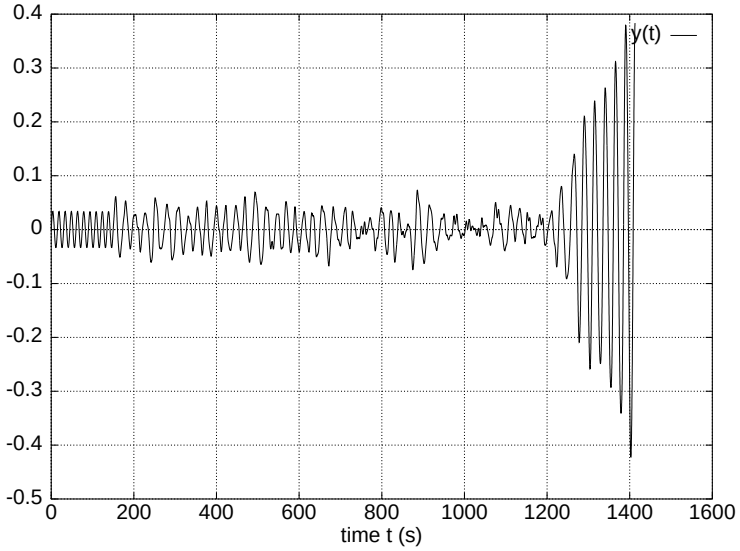

Figure 18: Rotation for free oscillations ($\theta_0 = 1.91$ deg, $T_s = 15s$).

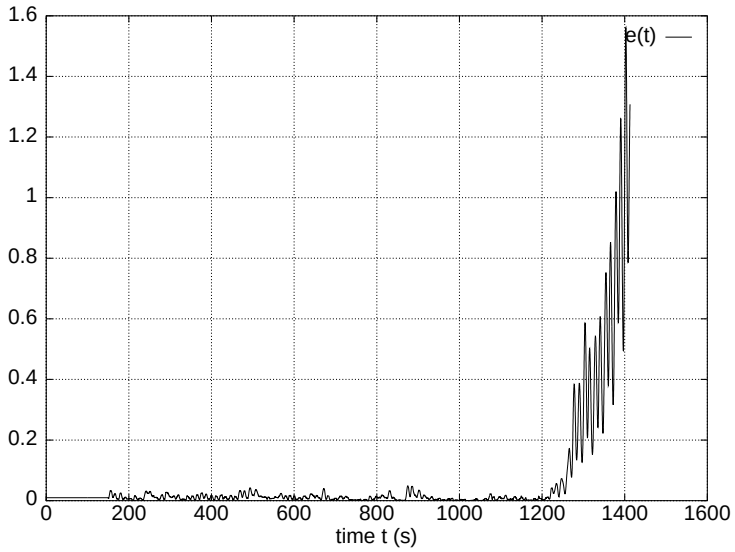

Figure 19: Structural energy for free rotation ($\theta_0 = 1.91$ deg, $T_s = 15s$).

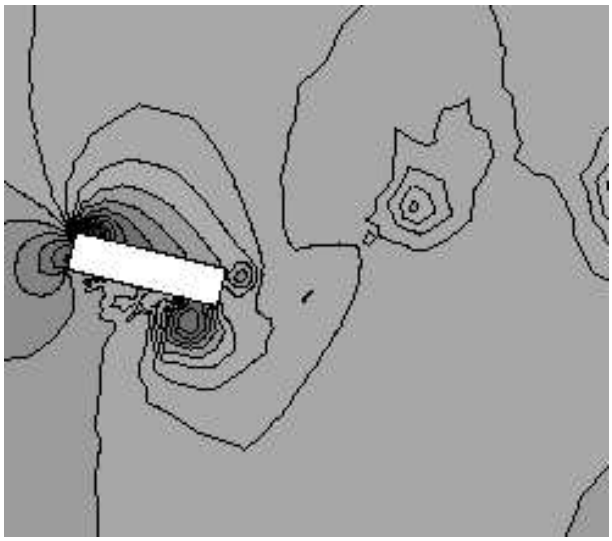

Figure 20: Pressure contours at maximal rotation for $T_s = 15$.

4.4 The Tacoma Narrows Bridge benchmark

The first Tacoma Narrows Bridge had an H-shaped cross section that is known to give rise to a phenomenon usually understood as vortex shedding, but more precisely called torsional

flutter [12]. For this kind of H-shaped decks, it has been observed that there is a slight tendency, as the height of the girder is reduced, for more airfoil-like effects to enter. However, for a girder depth as small as 0.1 the deck width, the tendency to instability remains strong. Scanlan and Tomko concluded that H-sections have very unfavorable aerodynamic stability characteristics [13].

The bridge collapsed at a critical wind speed of 18.8 m/s, after a support cable at mid-span was snapped by sufficiently large torsional undulations. The modeling of the deck as an H-shaped profile is supported by studies reviewed in [13]. The approximate geometry of this girder-stiffened type of deck is suggested on Figure 21.

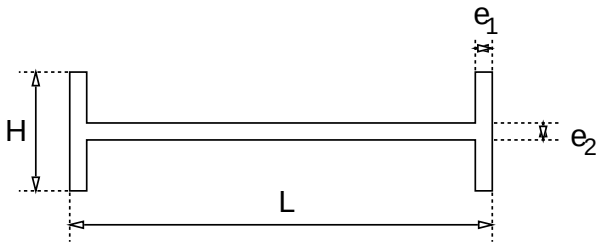

Figure 21: Approximate geometry of the Tacoma Narrows Bridge deck section.

For the geometry, we have chosen the following values:

$$\begin{cases} e_1 = e_2 = 1\ ft = 0.305\ m \\ H = 8\ ft = 2.438\ m \\ L = 39\ ft = 11.887\ m \end{cases} \tag{25}$$

Values for the structural model (1) and a reference where these values were recommended were found in [14]. We have taken:

$$\begin{cases} m = 8500\ kg/m, \\ I_\theta = 167344 Kg.m^2/m, \\ k_y = m\omega_y^2, \text{ with } f_y = \omega_y/2\pi = 0.84\ Hz, \\ k_\theta = I_\theta \omega_\theta^2, \text{ with } f_\theta = \omega_\theta/2\pi = 1.11\ Hz, \\ S_\theta = c_y = c_\theta = 0, \end{cases} \tag{26}$$

For the fluid flow, we have tested different values for the wind speed u_∞. We have taken for all computations

$$\begin{cases} \rho_\infty = 1.293\ Kg/m^3 \\ \nu = 1.496\ 10^{-5}\ m^2/s \end{cases} \tag{27}$$

The fluid domain around the deck section is discretized by an unstructured mesh of 7922 vertices and 22866 tetrahedra. The three dimensional domain again represents a one meter

slice around a one meter span section of the bridge. It was built by simple elevation starting from a 3961 vertex, 7622 triangle two-dimensional unstructured mesh, which is represented on Figure 22. This mesh is quite coarse (two elements for the discretization of the length e_1 of Figure 21). The final three dimensional mesh is made of 7922 vertices and 22866

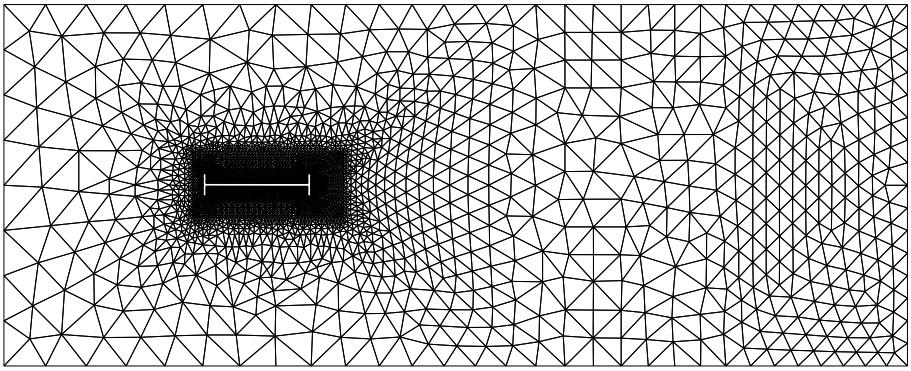

Figure 22: Discretization of the computational fluid domain.

tetrahedra. On this mesh, each of the following 30000 iteration computations required a computational time of four days on a DEC alpha 21164/500.

Numerical results are to be compared with experimental results presented for forced oscillations of the profile [13]. In this paper, no heaving instability and a torsional instability starting at $V = 28\ ms^{-1}$ are predicted. However, for free oscillation experiments with two degrees of freedom, as the wind speed increases, a heaving instability (induced by vortex shedding) should appear first, then disappear, and finally torsional flutter should take place.

We present here numerical results for free oscillation simulations with several wind speeds V in the range $[20.5; 40]$. For each test, the curves giving the vertical displacement y, the angle of rotation θ and the structural energy $e = (m\dot{y}^2 + k_y y^2 + I_\theta \dot{\theta}^2 + k_\theta \theta^2)/2$ are shown on Figures 23 to 26.

Many conclusions can be drawn from these plots. An instability in the heaving mode is clearly present in the range $V \in [23.18; 25]$. Out of this interval, the vertical displacement remains small. Similarly, no torsional flutter appears for $V < 32.5$. This conclusions are confirmed by energy plots. For $V = 23.18$ (Figure 23) and $V = 25$ (Figure 24), energy is transferred from the fluid to the structure, which is in a heaving mode. For $V \geq 32.5$ (Figure 25 and 26), energy is also stored by the structure, which is in torsional flutter. Out of these ranges, the structural energy is bounded (or increases much slower).

These conclusions are in very good agreement with experimental results reported in [13]. Numerical simulations have reproduced the two possible instabilities for this kind of profile: as the wind speed increases, a heaving instability first appears and disappears, and a torsional instability then takes place. This torsional flutter is a rather single-degree-of-freedom instability, as shown by the plots for the vertical displacement y in this range (see

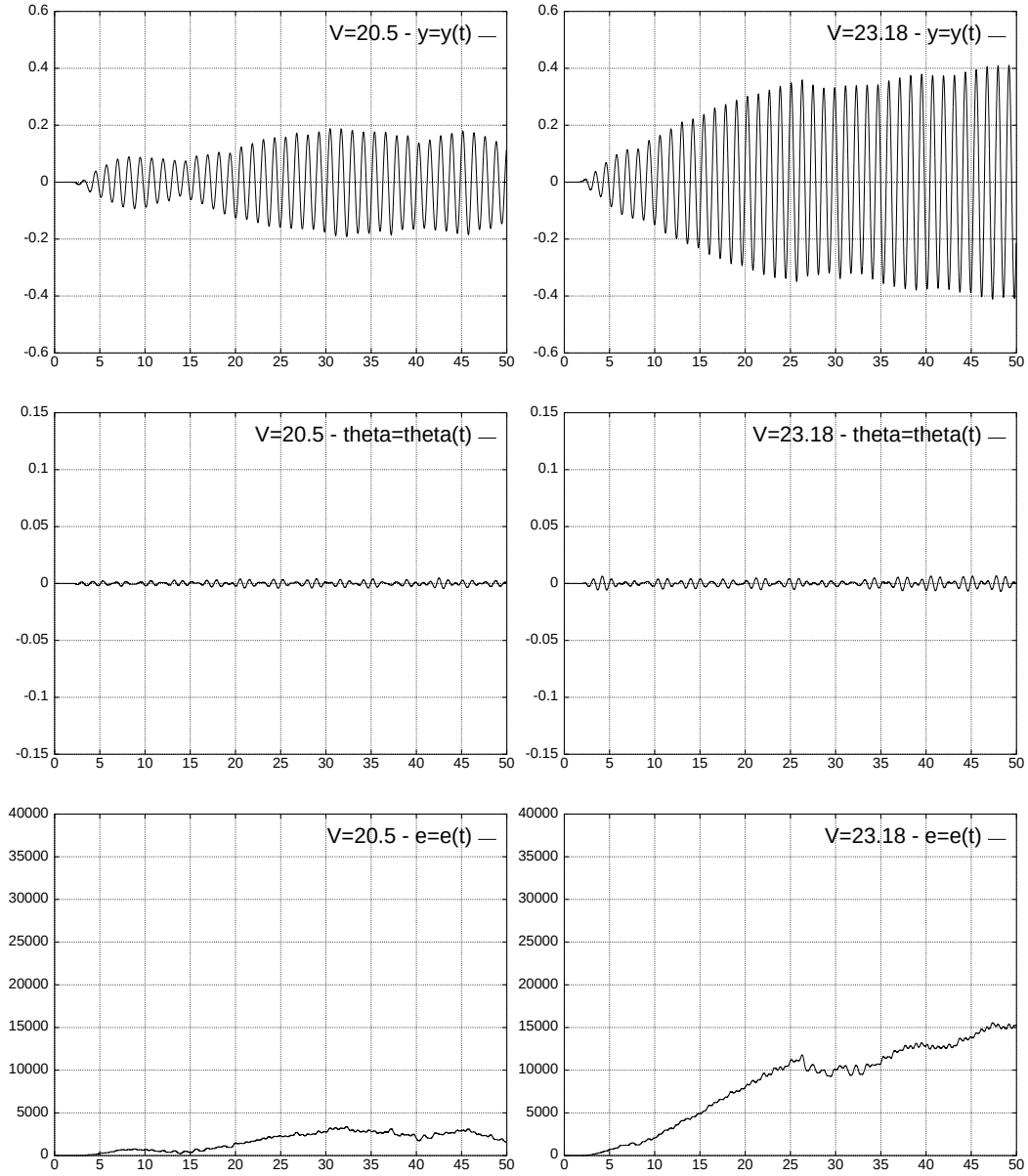

Figure 23: Displacement, rotation and energy for $V = 20.5$ and $V = 23.18$

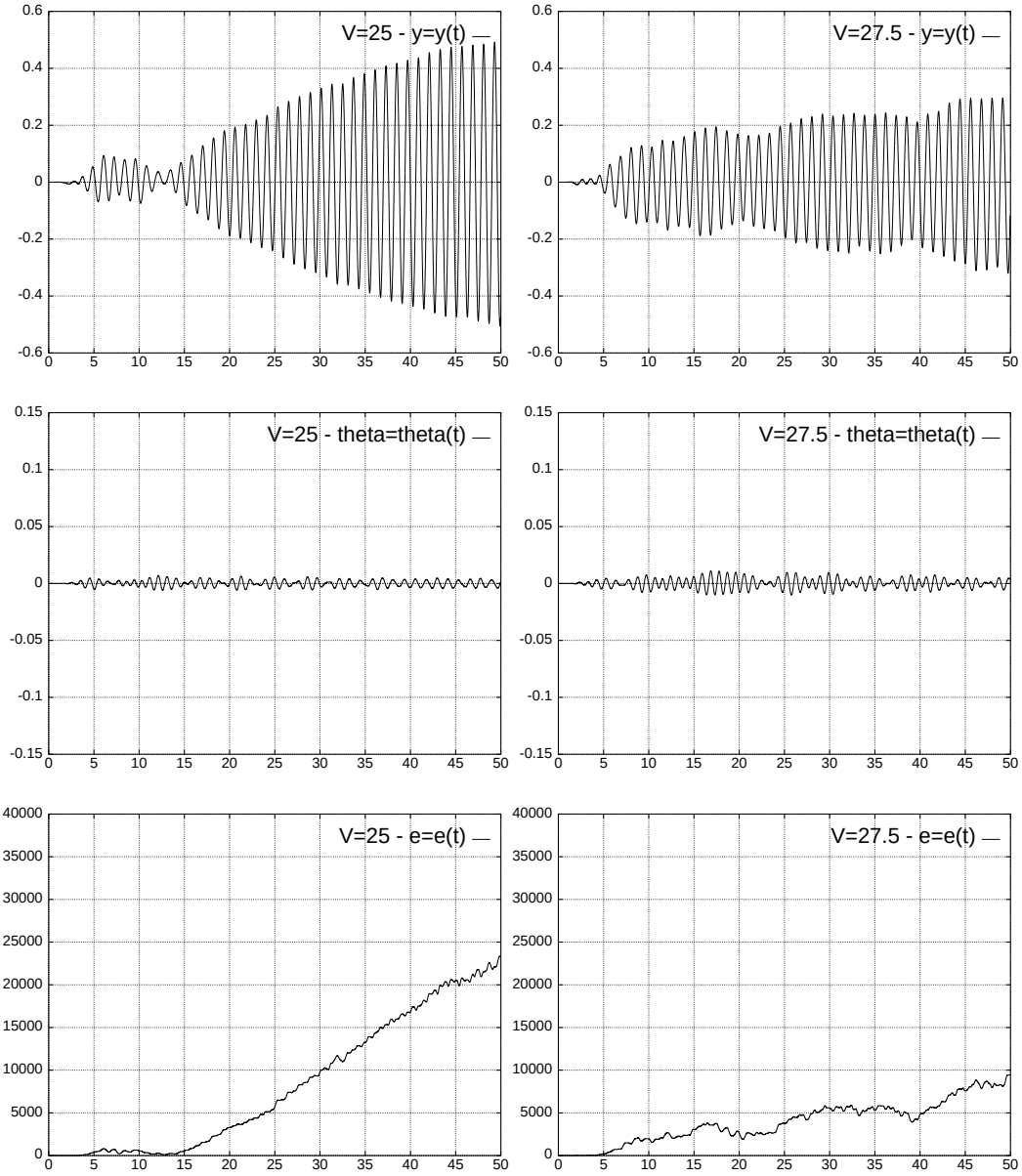

Figure 24: Displacement, rotation and energy for $V = 25$ and $V = 27.5$

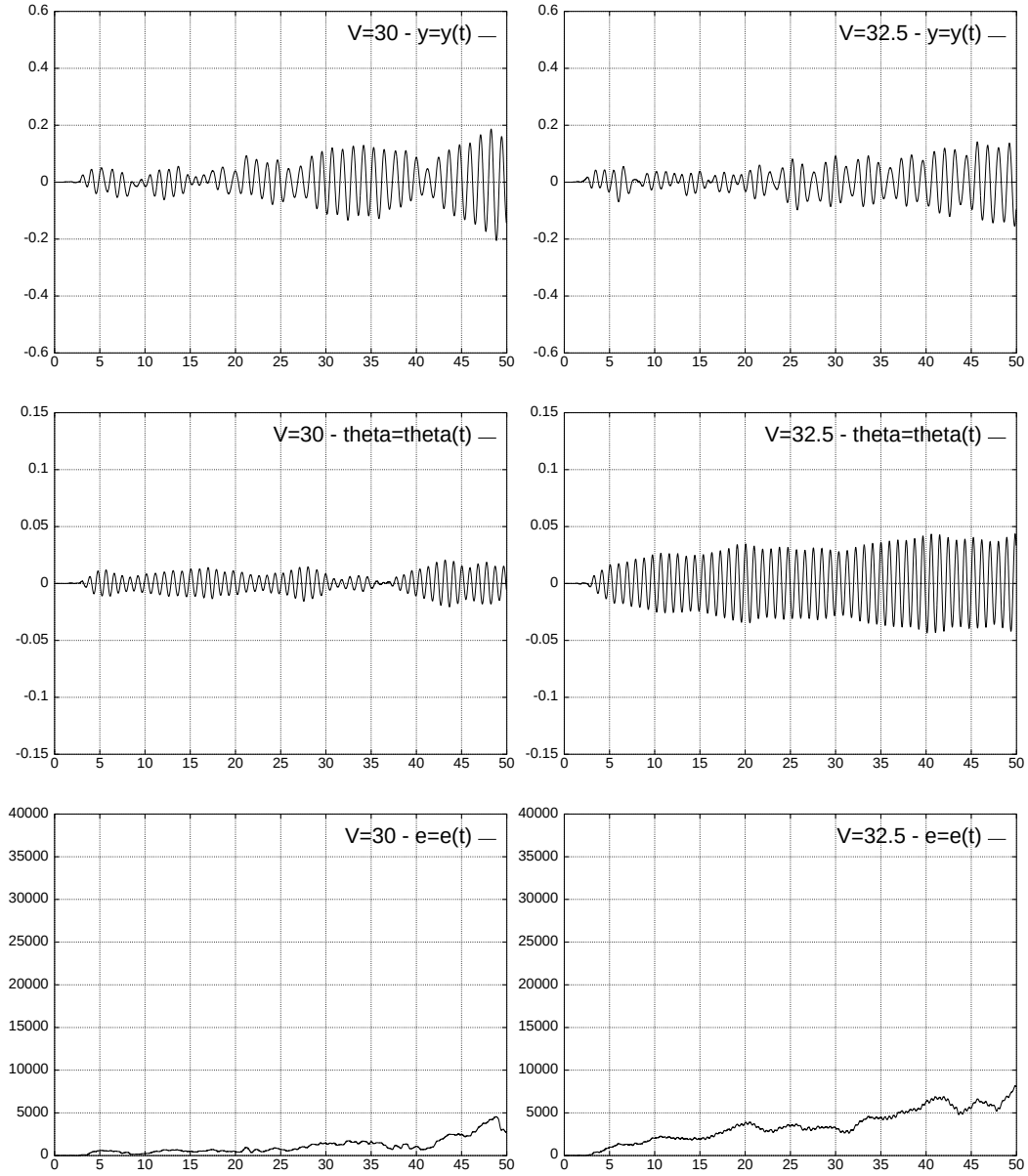

Figure 25: Displacement, rotation and energy for $V = 30$ and $V = 32.5$

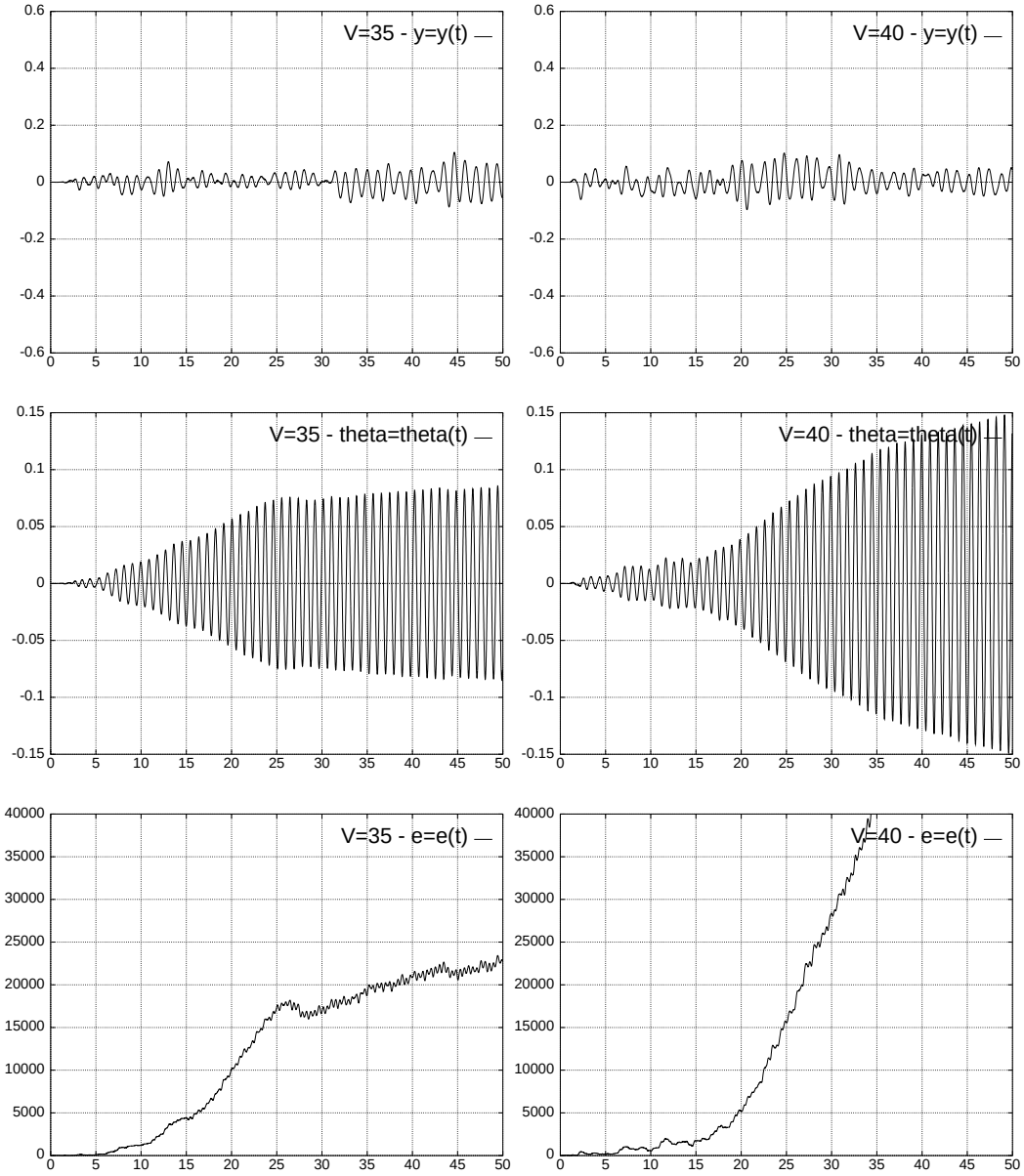

Figure 26: Displacement, rotation and energy for $V = 35$ and $V = 40$

Figure 26). However, on can wonder if some coupling between y and θ is present, at least in the range $V \in [32.5; 35]$, where torsional flutter appears. We have plotted on Figure 27 the

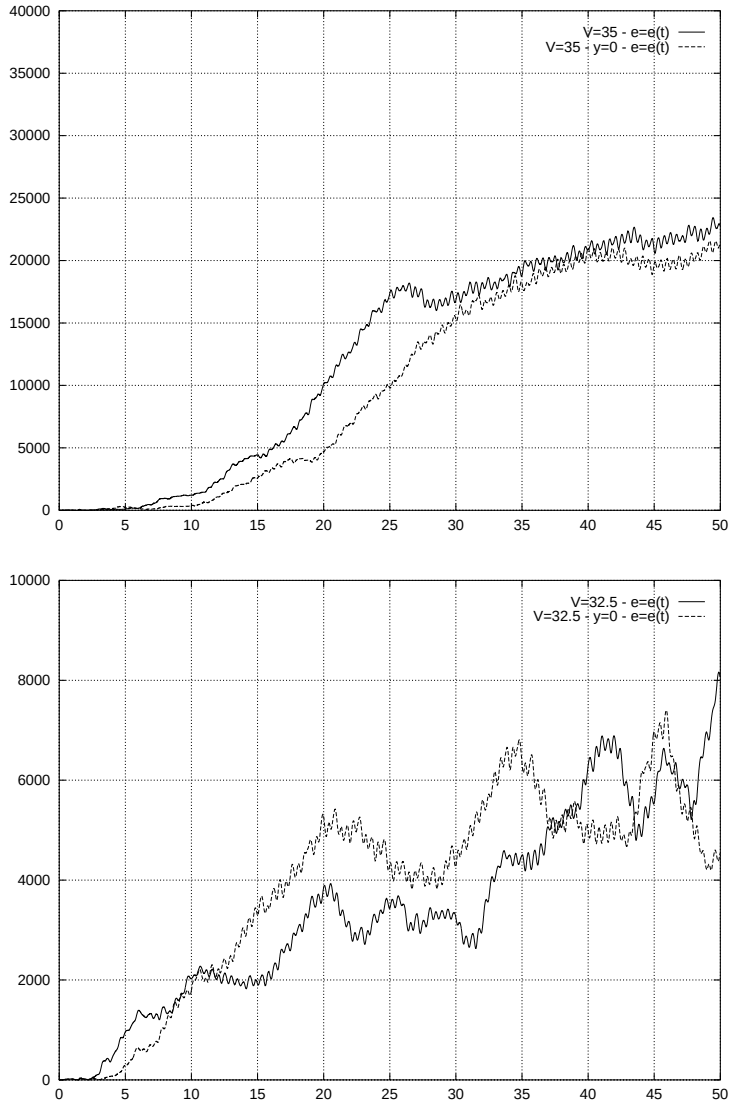

Figure 27: Energy for $V = 32.5$ and $V = 35$ with vertical displacement free or fixed.

structural energy for pairs of simulations with $V = 32.5$ and $V = 35$. The simulations labeled "y=0" are obtained with a simplified structural model reduced to the second equation of (1), i.e. the vertical displacement is fixed at $y = 0$. For each wind speed V, one can observe

that the structural energy is stored at the same rate for both simulations (y free or $y = 0$), but a little earlier when both degrees of freedom y and θ are present.

5 Conclusion

In this paper, we have reported numerical results for the simulation of the interaction of a viscous incompressible flow and rigidly moving sample bridge profiles.

We have presented simulations for both forced and free oscillations of the structure. On a rectangular cylinder, numerical results for forced oscillations have yielded satisfactory predictions for the possible instabilities. These predictions include the regime of instability as well as the amplitude in each unstable mode (heaving or torsional). However, the quantitative prediction for the stability limit in terms of the reduced speed $\mathbf{v}_m$ is not very accurate.

Free oscillation simulations gave results in very good coherence with forced oscillation simulations for the rectangle cylinder. For a H-section close to the profile of the Tacoma Narrows Bridge, numerical simulations have reproduced the heaving and torsional instabilities of the section, in satisfactory wind speed ranges.

These preliminary results were obtained with no turbulence model, and with an implicit first-order time-scheme which could produce artificial diffusion. Furthermore, the space and time discretizations were rather coarse. All these considerations lead us to be both satisfied with the results obtained and careful. More physical validations - especially three-dimensional and with flexible structures - are needed to obtain a reliable simulator for this type of fluid-structure interactions.

References

[1] D. Arnold, F. Brezzi, and M. Fortin. A stable finite element for the stokes equations. *Calcolo*, 21(4):337–344, 1984.

[2] J.T. Batina. Unsteady euler airfoil solutions using unstructured dynamic meshes. *AIAA J.*, 28:1381–1388, August 1990.

[3] P.G. Ciarlet. *The Finite Element Method for Elliptic Problems*. North Holland-Elsevier Science Publishers, Amsterdam, New York, Oxford, 1978.

[4] Y. Lecointe and J. Piquet. On the use of several compact methods for the study of unsteady incompressible viscous flow round a circular cylinder. *Comput. & Structures*, 12(4):255–280, 1984.

[5] M. Lesoinne and C. Farhat. Stability analysis of dynamic meshes for transient aeroelastic computations. In *11th AIAA Computational Fluid Dynamics Conference, Orlando, Florida*, July 6-9 1993. AIAA paper 93-3325.

[6] T. Nomura and T. Hughes. An arbitrary lagrangian-eulerian finite element method for interaction of fluid and a rigid body. *Comput. Methods Appl. Mech. Engrg.*, 95:115–138, 1992.

[7] Y. Otsuki, K. Washizu, H. Tomizawa, and A. Ohya. A note on the aeroelastic instability of a prismatic bar with square section. *J. Sound Vibration*, 34(2):233–248, 1974.

[8] C. Pares Madronal. *Etude mathématique et approximation numérique de quelques problèmes aux limites de la mécanique des fluides.* PhD thesis, Université de Paris VI, 1992.

[9] S. Piperno. Two-dimensional euler aeroelastic simulations with interface matching relaxation. In J.-A. Désidéri, P. Le Tallec, E. Oñate, J. Périaux, and E. Stein, editors, *Proceedings of the Second ECCOMAS Conference on Numerical Methods in Engineering*, pages 898–904, Paris, France, September 9-13 1996. John Wiley & Sons.

[10] S. Piperno. Explicit/implicit fluid/structure staggered procedures with a structural predictor and fluid subcycling for 2d inviscid aeroelastic simulations. *Internat. J. Numer. Methods Fluids*, 25:1207–1226, 1997.

[11] O. Pironneau. *Méthodes des éléments finis pour les fluides.* Collection Recherches en Mathématiques Appliquées. Masson, Paris, 1988.

[12] R.H. Scanlan. On the state of stability considerations for suspended-span bridges under wind. In *Proceedings IUTAM-IAHR Symposium*, pages 595–618, Karlsruhe, Germany, 1979.

[13] R.H. Scanlan and J.J. Tomko. Airfoil and bridge deck flutter derivatives. *Journal of the Engineering Mechanics Division, ASCE*, 97(EM6):1717–1737, December 1971.

[14] H. Tran, B. Koobus, and C. Farhat. Numerical simulations of vortex shedding flows past moving obstacles using the $k - \varepsilon$ turbulence model on unstructured dynamic meshes. Technical Report 97-16, Center for Aerospace Structures, University of Colorado, Boulder, Colorado, October 1997.

[15] K. Washizu, A. Ohya, Y. Otsuki, and K. Fujii. Aeroelastic instability of rectangular cylinders in a heaving mode. *J. Sound Vibration*, 59(2):195–210, 1978.

[16] K. Washizu, A. Ohya, Y. Otsuki, and K. Fujii. Aeroelastic instability of rectangular cylinders in a torsional mode due to a transverse wind. *J. Sound Vibration*, 72(4):507–521, 1980.

Unité de recherche INRIA Sophia Antipolis
2004, route des Lucioles - B.P. 93 - 06902 Sophia Antipolis Cedex (France)

Unité de recherche INRIA Lorraine : Technopôle de Nancy-Brabois - Campus scientifique
615, rue du Jardin Botanique - B.P. 101 - 54602 Villers lès Nancy Cedex (France)
Unité de recherche INRIA Rennes : IRISA, Campus universitaire de Beaulieu - 35042 Rennes Cedex (France)
Unité de recherche INRIA Rhône-Alpes : 655, avenue de l'Europe - 38330 Montbonnot St Martin (France)
Unité de recherche INRIA Rocquencourt : Domaine de Voluceau - Rocquencourt - B.P. 105 - 78153 Le Chesnay Cedex (France)

Éditeur
INRIA - Domaine de Voluceau - Rocquencourt, B.P. 105 - 78153 Le Chesnay Cedex (France)
http://www.inria.fr
ISSN 0249-6399